Communications Materials

https://doi.org/10.1038/s43246-025-01046-0

Article in Press

Multiscale insights enable rational design of solvent-free dry electrode processing for advanced battery electrode fabrication

Received: 11 July 2025

Accepted: 11 December 2025

[redacted]

Cite this article as: Kang, J.H., Jeong, W., Kang, M.S. *et al.* Multiscale insights enable rational design of solvent-free dry electrode processing for advanced battery electrode fabrication. *Commun Mater* (2025). https://doi.org/10.1038/s43246-025-01046-0

Jun Hyuk Kang, Woojin Jeong, Min Sung Kang, Hyeon Woo Kim, Dong Won Jeon, Han Uk Lee, Ji Hoon Hong, Seungmin Han, Minseok Kim, Subi Yang, Dongsoo Lee, Patrick Joohyun Kim, Taeseup Song, Moonsu Yoon, Laisuo Su, Junghyun Choi & Sung Beom Cho

We are providing an unedited version of this manuscript to give early access to its findings. Before final publication, the manuscript will undergo further editing. Please note there may be errors present which affect the content, and all legal disclaimers apply.

If this paper is publishing under a Transparent Peer Review model then Peer Review reports will publish with the final article.

ARTICLE IN PRESS

© The Author(s) 2025. **Open Access** This article is licensed under a Creative Commons Attribution-NonCommercial-NoDerivatives 4.0 International License, which permits any non-commercial use, sharing, distribution and reproduction in any medium or format, as long as you give appropriate credit to the original author(s) and the source, provide a link to the Creative Commons licence, and indicate if you modified the licensed material. You do not have permission under this licence to share adapted material derived from this article or parts of it. The images or other third party material in this article are included in the article's Creative Commons licence, unless indicated otherwise in a credit line to the material. If material is not included in the article's Creative Commons licence and your intended use is not permitted by statutory regulation or exceeds the permitted use, you will need to obtain permission directly from the copyright holder. To view a copy of this licence, visit http://creativecommons.org/licenses/by-nc-nd/4.0/.

Multiscale Insights Enable Rational Design of Solvent-Free Dry Electrode Processing for Advanced Battery Electrode Fabrication

Jun Hyuk Kang[a,b†], Woojin Jeong[c†], Min Sung Kang[a,b], Hyeon Woo Kim[b,d], Dong Won Jeon[a,b], Han Uk Lee[a,b], Ji Hoon Hong[a,b], Seungmin Han[c], Minseok Kim[e], Subi Yang[f], Dongsoo Lee[e], Patrick Joohyun Kim[f], Taeseup Song[c], Moonsu Yoon[e], Laisuo Su[g], Junghyun Choi[e*], and Sung Beom Cho[a,b,d*]

[a]Department of Energy Systems Research, Ajou University, Suwon 16499, Republic of Korea

[b]Department of Materials Science and Engineering, Ajou University, Suwon 16499, Republic of Korea

[c]Department of Energy Engineering, Hanyang University, 222 Wangsimni-ro, Seongdong-gu, Seoul 04763, Republic of Korea

[d]Ajou Energy Science Research Center, Ajou University, Suwon 16499, Republic of Korea

[e]School of Chemical, Biological and Battery Engineering, Gachon University, Seongnam-si, Gyeonggi-do 13120, Republic of Korea

[f]Department of Applied Chemistry, Kyungpook National University, Daehak-ro 80, Buk-gu, Daegu 41566, Republic of Korea

[g]Department of Materials Science and Engineering, The University of Texas at Dallas, Richardson, Texas 75080, United States

*Corresponding authors: junghchoi@gachon.ac.kr and csb@ajou.ac.kr

Abstract

High-performance electrodes can be fabricated using environmentally friendly dry processes instead of wet processes. A key material in dry processing is polytetrafluoroethylene (PTFE), which fibrillates under shear stress and forms a robust fibrous network essential for electrode integrity. However, the precise control of PTFE fibrillation is challenging owing to the complex transfer of shear forces from macroscale equipment to microscale particle dynamics. To address this, we present a multiscale optimization framework integrating finite element method simulations, Gaussian process regression, and Bayesian optimization to engineer PTFE fibrillation. Our model identifies the optimal particle size and particle-loaded pressure. It demonstrates that a 10+5 μm bimodal system with 14 MPa of particle-loaded pressure yields the most effective fibrillation. Electrodes are inversely designed using 10+5 μm particles, and enhanced electrochemical properties are experimentally validated. The proposed optimized dry electrode fabrication bridges microscale particle dynamics with large-scale processing.

Keywords: Dry process, PTFE fibrillation, Optimization, Inverse design, FEM simulations, Machine-learning tools.

Introduction

The growing demand for Li-ion batteries (LIBs) in electric vehicles (EVs) and energy storage systems (ESS) necessitates batteries with higher energy capacities.[1] To satisfy this demand, advancements in battery technology have been made to enhance the cell energy density by fabricating thicker electrodes with uniform particle distribution, which improve both the energy storage capacity and structural stability of the battery.[2,3] However, conventional wet processes induce binder migration during solvent evaporation, resulting in nonuniform particle distribution and unavoidable difficulties in manufacturing thick electrodes.[4] To overcome these challenges, the solvent-free dry process has emerged as a promising alternative.[5–9] This method employs polytetrafluoroethylene (PTFE) as a binder that fibrillates under shear stress, forming a fibrous network that connects active material particles without a solvent. The absence of solvents renders the process more ecofriendly by eliminating toxic vapor emissions while significantly reducing production costs and energy consumption.[10,11] Moreover, a well-developed PTFE fiber network ensures uniform particle distribution within structurally robust thick electrodes.[12] Nevertheless, achieving a homogeneous PTFE fiber network during the dry process remains challenging. Therefore, the processing conditions must be optimized to ensure a uniform granule structure and fully realize the benefits of dry electrode fabrication.

The formation of a fiber network is primarily governed by shear stress, and this fiber network determines the electrode performance by binding active materials and conductive agents.[13,14] During granule formation, shear stress applied through kneading or extrusion promotes PTFE fibrillation, thereby creating a fibrous network that strongly binds active materials (AMs) and conductive agents.[15] The extent of fibrillation substantially impacts the particle distribution uniformity, ultimately determining whether the electrode exhibits brittle However, precise control of the mechanical properties remains challenging because the formation of the PTFE fiber network is highly sensitive to processing parameters. For example, an insufficient kneading time limits PTFE deformation, resulting in inadequately formed electrode granules. In contrast, an excessive kneading time causes over-deformation, altering the fibrous structure into a film-like morphology and thus making the resulting dough brittle and prone to fracture.[16] Therefore, achieving dry-processed electrodes with enhanced mechanical properties through PTFE fibrillation requires an in-depth understanding of the interactions between microscopic dynamics and macroscopic processing conditions.

During the dry process, surrounding particles exert microscale forces on PTFE particles, which play a crucial role in initiating and controlling fibrillation.[17] This particle-level fibrillation is governed by macroscale parameters such as temperature,[8] rotational speed,[18] and processing time.[19] However, the limited understanding of the correlation between microscale particle dynamics and macroscale process parameters hinders the precise control of PTFE fibrillation, which consequently limits the development of optimized dry electrodes. Previous studies have primarily explored PTFE fibrillation mechanisms through rheological analyses.[20] However, such approaches may fail to fully capture the particle–PTFE interactions that drive deformation in the solvent-free dry process. Therefore, designing an optimized dry process requires an appropriate theoretical framework and process design strategy based on fundamental understanding of efficient PTFE fibrillation.[21]

In this study, we developed an artificial intelligence (AI)-based multiscale optimization framework to fabricate dry-processed electrodes with a uniform microstructure and an areal capacity of 10 mAh cm^{-2} by precisely controlling PTFE. This framework integrates a finite element method (FEM)-based microscale particle dynamics model employing nonlinear solid mechanics to analyze the deformation behavior of the PTFE binder under shear stress during dry processing. This approach accurately captures the strain-dependent fibrillation characteristics of PTFE,[22–24] enabling a mechanistic understanding of microscale particle dynamics in solvent-free dry processes. The simulation results were experimentally validated, confirming a clear correlation between active material particle size and PTFE fibrillation behavior. Furthermore, Gaussian process regression (GPR) was applied to the FEM results to interpolate the relationship between process conditions and microscale responses,[25,26] and Bayesian optimization[27] was used to systematically identify macroscale kneader and extruder operating conditions, thereby bridging the gap between microscale deformation behavior and large-scale process parameters. Building on these insights, we further extended the framework to inverse process design, achieving optimized PTFE control. We anticipate that this framework will act as a transformative "game changer" for dry electrode manufacturing, significantly reducing production costs. The findings provide fundamental insights into dry electrode processes and offers practical guidelines for LIBs development.

Results and Discussion

Multiscale PTFE fibrillation design

Fig. 1a illustrates the dry electrode manufacturing process and the impact of PTFE fibrillation on electrode performance. During granule formation, PTFE serves as a binder that fibrillates under shear stress, forming a fibrous network that effectively binds active material particles. When the PTFE fibrous network is well-developed, the resulting electrode exhibits robust mechanical integrity. Conversely, insufficient or fragmented PTFE fibrillation leads to weak particle bonding, resulting in a brittle electrode with poor mechanical properties, which can ultimately lead to electrode fracture during the process. This comparison highlights the critical importance of achieving optimal PTFE fibrillation for stable electrode fabrication. Following this, **Fig. 1b** shows the workflow of a multiscale approach for optimizing PTFE fibrillation. First, nonlinear structural mechanics[28] FEM simulations are conducted to analyze microscale particle dynamics under varying particle size and particle-loaded pressure (PLP). From these simulations, we extract the second Piola–Kirchhoff stress (P_{lm}) and strain values. P_{lm} accurately reflects stress under large deformation conditions, which are inherent to the fibrillation of PTFE due to its high-strain behavior.[29,30] These values are used to train a GPR model, whose inputs are the particle size and PLP, and the P_{lm} and strain values are predicted as outputs. The trained GPR model enables the identification of optimal PLP conditions per particle size.[31] Finally, an inverse design approach translates the optimal conditions into a macroscale granule formation process, and experimental validation of the designed process parameters is performed.

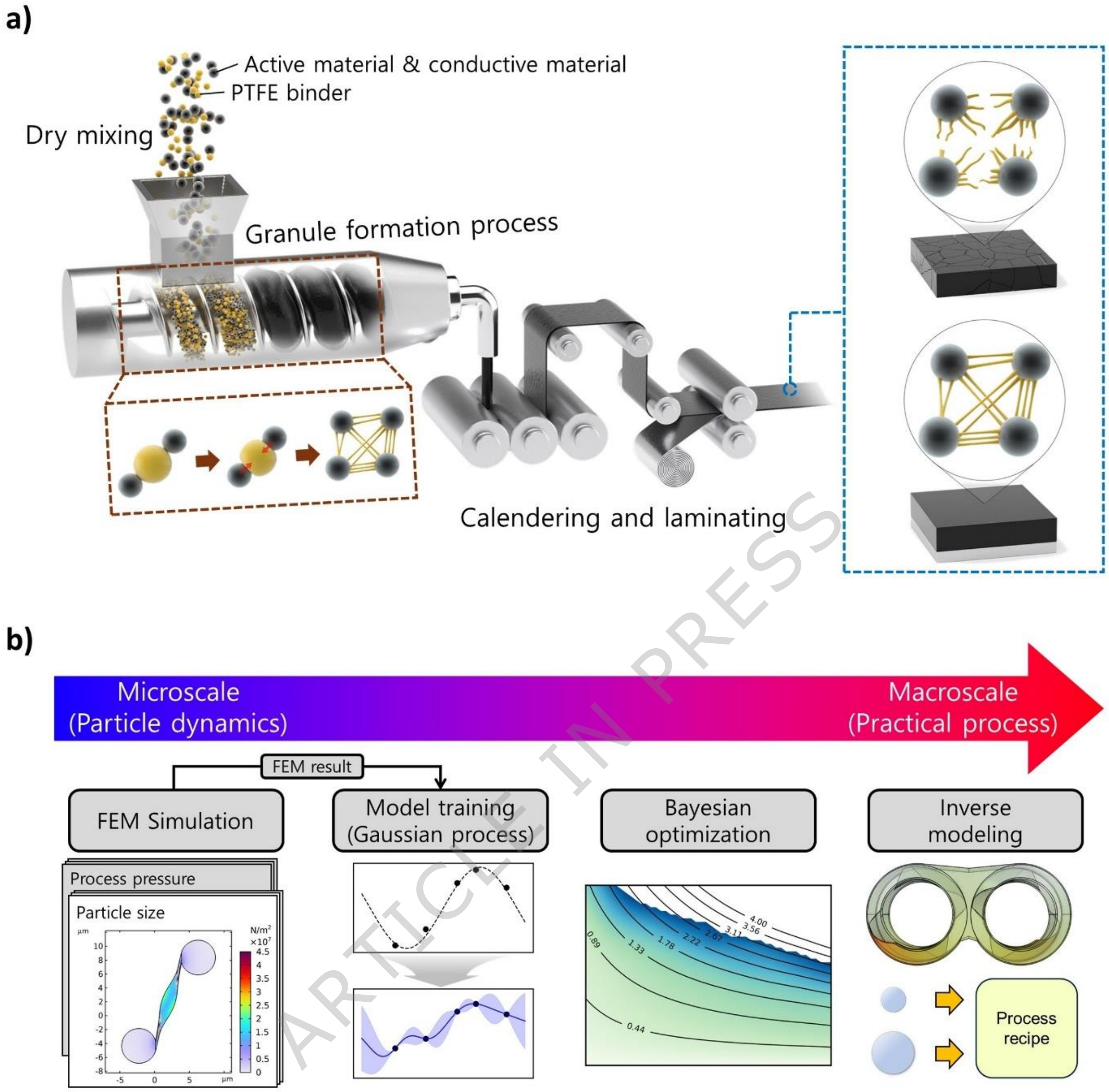

Fig. 1 | Multiscale inverse design framework for optimizing PTFE fibrillation in dry electrode processing.

a Schematic illustration of the dry electrode manufacturing process and the effect of PTFE fibrillation on electrode. **b** Workflow of computational process for efficient PTFE fibrillation.

Simulation for PTFE deformation

The particle dynamics model used to analyze PTFE fibrillation behavior is illustrated in **Fig. 2a**. The model comprises ceramic AMs and PTFE particles, where each ceramic AM exerts PLP, generating shear force within the PTFE matrix. This simulation yields the stress–strain (SS) curve, which divides the PTFE deformation into four distinct regions (**Fig. 2b**). Region I represents the elastic deformation characterized by linear SS behavior. In Region II, PTFE undergoes plastic deformation, exhibiting nonlinear stress accumulation. Region III corresponds to fibrillation, where shear-induced deformation leads to fiber formation. If the applied stress exceeds the PTFE tensile strength, the fibrillar structure collapses into the film-like[8] morphology of Region IV, indicating over-deformation and loss of the fibrillar structure. These results align closely with previous studies on PTFE fibrillation under high strain.[32,33] To quantitatively validate our finite-element model, we compared the simulated SS curve with experimental data from the literature. This comparison confirmed that our model accurately captures the key features of PTFE's initial mechanical response required for fibrillation. Specifically, the simulated and experimental curves agreed in the elastic-to-plastic transition. Additionally, the model identifies the fibrillation onset at a strain of 1.13 (Region III, Fig. 2b), where the simulated stress was 16.9 MPa—a value comparable to the experimental result of 16.4 MPa value comparable to the experimental result of 16.4 MPa. While the ultimate elongation at failure differs between the datasets, which is likely due to variations between the PTFE grades used, the close agreement in the critical elastic and initial plastic-deformation regions provides robust validation for our model's primary objective: predicting the onset of fibrillation.[34]”

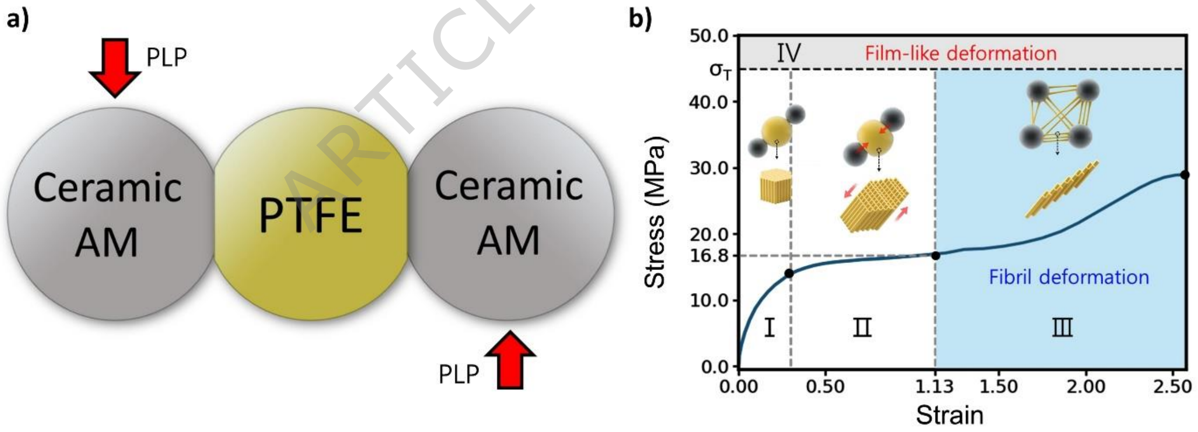

Fig. 2 | Simulation for PTFE deformation. a Schematic of the boundary conditions and initial state in the simulation. **b** SS curve of PTFE illustrating fibrillation evolution and transition to film-like deformation.

Particle-size-dependent PTFE fibrillation behavior

We analyzed the effect of the AM particle size on PTFE fibrillation using the FEM model and ex perimentally validated the results using SiO_2 particles. SiO_2 was selected because it can be synthesized with uniform particle size distribution (PSD)[34] and a perfectly spherical shape, considerably simplifying particle size control. **Fig. 3a** presents the particle size analysis results, confirming the frequency distributions of unimodal SiO_2 particles (0.1, 1.5, 10, and 20 μm) used in this study. **Fig. 3b** shows the SS curves for different SiO_2 particle sizes (0.1, 1.5, 10, and 20 μm) under 13 MPa, while the corresponding FEM simulation results are presented in **Supplementary Fig. 1**. To investigate the effect of PTFE fiber morphology on the mechanical properties of dry films with different particle sizes, a universal testing machine (UTM) measurement was conducted, revealing that the variation in fibrillation efficiency with particle size is directly reflected in the mechanical integrity, as shown in **Fig. 3c**. For 20 μm particles, the SS curve extends into the failure region, indicating that the applied stress exceeds the PTFE tensile strength and induces a film-like morphology. This behavior is confirmed experimentally as shown in **Fig. 3d**. In contrast, 10 μm particles generate adequate stress and strain to initiate fibrillation without exceeding the material tensile strength. The S-S curve for these particles confirms this behavior, exhibiting a yield point (indicated by the circle symbol in Fig**. 3b**) at approximately 27 MPa (strain = 0.6) and an onset of robust fibrillation (square symbol) at a peak stress of 30 MPa (strain = 1.8), with the entire process occurring well below the tensile strength of 45 MPa. The S-S curve for these particles shows a distinct pattern characteristic of semicrystalline polymers, reflecting the strain-induced orientation of polymer chains. This behavior is experimentally validated as shown in **Fig. 3e**. For intermediate sizes, 1.5 µm particles facilitate electrode granule formation but fail to induce sufficient PTFE fibrillation. This is evidenced by both the scanning electron microscopy (SEM) images in Fig. **3f** and their S-S curve, which does not enter the region associated with fibrillation. By contrast, 0.1 µm particles generate insufficient stress to progress beyond the elastic deformation region, as the limited contact area restricts stress transfer and the extremely narrow interparticle spacing confines the deformation space of PTFE chains, consistent with **Fig. 3g**. Consequently, the resulting dry film exhibits a brittle nature. These findings demonstrate that the particle size significantly influences PTFE fibrillation. **Fig 3h** presents the porosity of unimodal dry electrodes. The 20 μm electrode exhibited a film-like PTFE distribution that slightly reduced micropores but resulted in relatively high porosity (37.2%) due to non-uniform fibrillation. In contrast, the 10 μm electrode showed uniform PTFE fibrillation, forming a dense structure with low porosity. For the 1.5 μm electrode, reduced flowability and limited stress transfer caused PTFE to become tra pped within agglomerates, preventing uniform interparticle connections and leading to increased micropore formation and overall porosity. As shown in *Supplementary Fig. 2*, the tap density gradually decreased with decreasing particle size. This is attributed to the increased specific surface area and particle agglomeration of smaller particles, which reduce powder flowability and packing efficiency. Ideal-sized particles (e.g., 10 µm) effectively promote PTFE fibrillation by supplying sufficient shear stress at contacts, resulting in a well-developed fibrous network (**Fig. 3j**). This is validated by their S-S curves successfully reaching the target fibrillation region. By contrast, smaller particles (e.g., 0.1 µm) fail to generate sufficient stress due to reduced pressure at each contact point (**Fig. 3k**), as evidenced by their S-S curves remaining in the low-stress region. Conversely, large particles (e.g., 20 µm) cause over-deformation by concentrating stress beyond the material's tensile strength (**Fig. 3i**), corresponding to the failure region. Therefore, optimal particle size selection, approximately within the 5–10 µm range, is essential for fabricating electrode granules with efficient PTFE fibrillation and desirable mechanical properties.

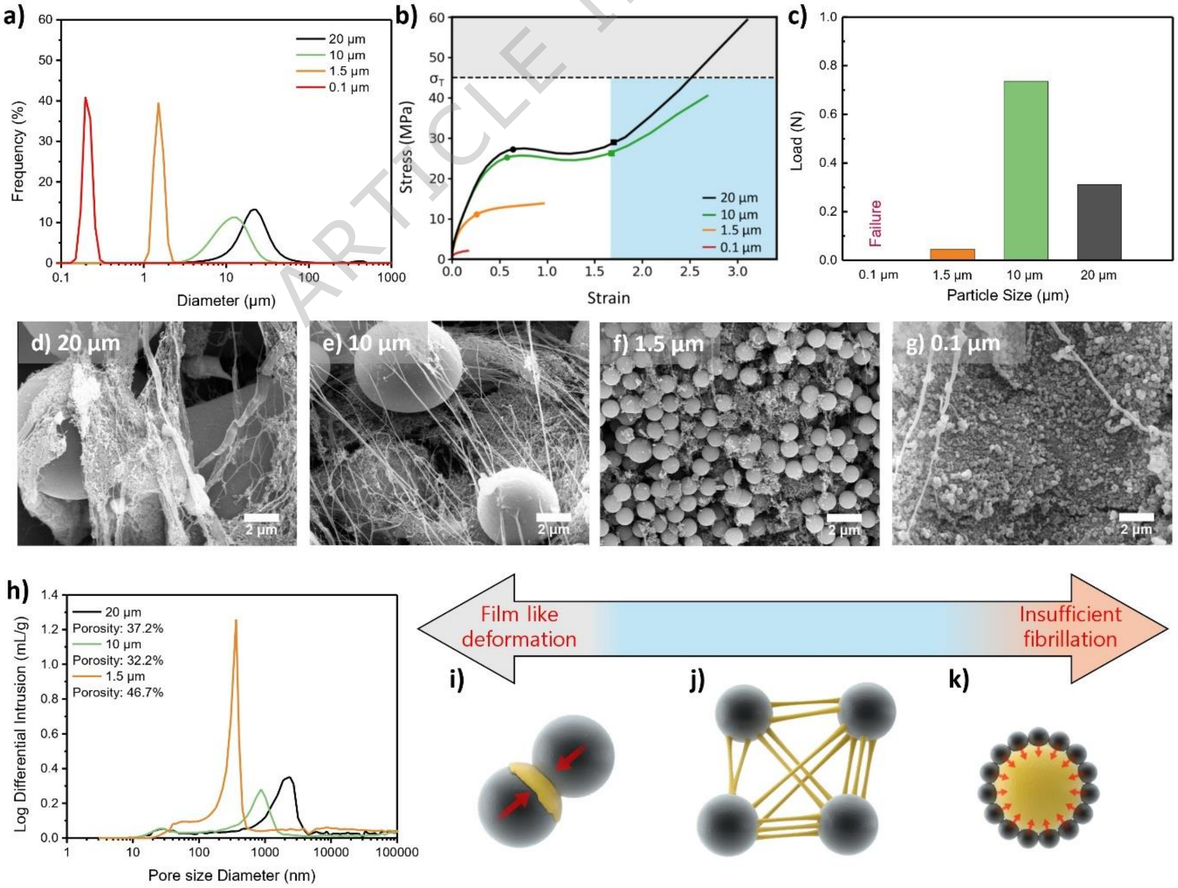

Fig. 3 | Correlating FEM-based stress response with experimental validation of unimodal particle size effects. a Frequency distribution of unimodal SiO_2 particles with nominal diameters of 0., 1.5, 10, and 20 µm, measured using a laser-scattering PSD analyzer. **b** SS curves for different SiO_2 particle sizes. The blue area indicates the target fibrillation region, and the gray area represents the failure region leading to film-like deformation. The circle and square symbols on the SS curve denote the yield point and the onset of fibrillation, respectively. **c** Cohesive-strength test results. **d–g** SEM images of samples containing SiO_2 particles with sizes of (**d**) 20, (**e**) 10, (**f**) 1.5, and (**g**) 0.1 µm. **h** Mercury intrusion porosimetry results for dry electrodes prepared with unimodal SiO_2 particles of different median sizes. Reliable porosity measurement for the dry electrode fabricated with 0.1-µm SiO_2 particles was impossible owing to its brittle nature. **i–k** Schematic of the effect of the particle size on the PTFE deformation behavior. **(i)** Film-like deformation. **(j)** Fibrillation. **(k)** Insufficient fibrillation.

Optimizing PTFE fibrillation via bimodal PSDs

Building upon the findings from the unimodal evaluation, we further investigated PTFE deformation under bimodal PSDs to clarify the influence of particle size on fibrillation. For this analysis, we combined two particle sizes, always including 10-µm SiO_2, which was previously identified as the optimal size for PTFE fibrillation. The particle size analysis of the bimodal systems (10+5 µm and 10+1.5 µm) is shown in **Fig. 4a**, where their respective frequency distributions are presented. **Figs. 4b–j** show results for bimodal PSDs, with 10-µm SiO_2 combined with either 5- or 1.5- µm SiO_2 particles under 13 MPa. **Fig. 4b** shows the SS curve for these particle size combinations. Both the unimodal 10 µm particles and 10+5 µm combination deliver sufficient stress and strain to initiate fibrillation without exceeding the PTFE tensile strength, as confirmed by the SEM images in **Figs. 4d and 4e**. Notably, the 10+5 µm combination exhibits enhanced fibrillation, corresponding to a 7.4% increase, compared with the unimodal distribution, likely due to improved particle packing and efficient stress transfer, which facilitate the formation of the PTFE network. This superior fibrillation directly translates to mechanical integrity, as shown in **Fig. 4c**, where the 10+5 µm bimodal combination exhibits the highest cohesive strength. In contrast, the 10+1.5 µm combination facilitates electrode granule formation, as indicated by the SS curve, while the SEM image in **Fig. 4f** reveals insufficient PTFE fibrillation. Smaller particles (1.5 µm) appear to concentrate stress unevenly, hindering uniform fiber development. These results highlight that overly broad PSDs lead to inefficient fibrillation owing to the dominance of smaller particles. In contrast, an optimized particle size combination, such as 10+5 µm, efficiently improves fibrillation by balancing the applied stress and strain within the PTFE deformation range. In **Fig. 4c**, the 10+5 µm bimodal combination exhibits the highest cohesive strength, indicating that appropriate particle size design is crucial for fabricating optimal electrodes. **Fig. 4g** shows that in the bimodal system, the 10+1.5 μm sample still exhibited numerous micropores, whereas the optimized 10+5 μm combination showed a lower porosity. In addition, as the secondary-particle size increased from 1.5 to 5 μm, the tap density increased from 1.18 to 1.40 g cm^{-3} (**Supplementary Fig. 3**). This indicated that intermediate-sized particles effectively filled the gaps between larger particles, enhancing the packing efficiency and homogenizing stress transfer, which enabled more uniform PTFE fibrillation. **Figs. 4h–j** illustrate the PTFE fibrillation mechanism described in this paragraph. Careful control of the PSD is crucial for optimizing PTFE fibrillation, stress transfer, and electrode structural integrity.

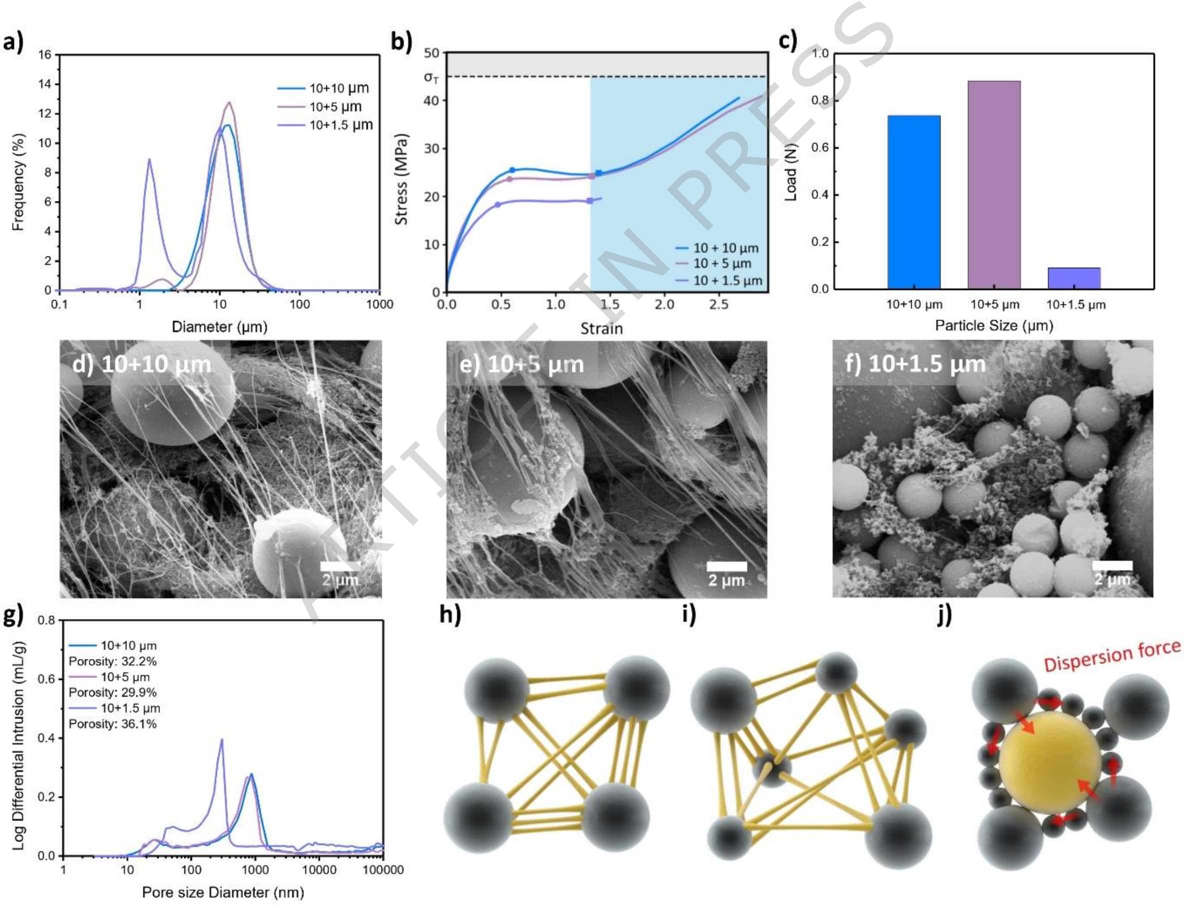

Fig. 4 | Correlating FEM-based stress response with experimental validation of bimodal particle size effects. a Frequency distribution of bimodal SiO_2 systems with particle size combinations of 10+1.5 μm and 10+5 μm, measured using a laser-scattering PSD analyzer. **b** SS curves for different SiO_2 particle size combinations. The blue area indicates the target fibrillation region, while the gray area represents the failure region leading to film-like deformation. The circle and square symbols on the SS curve denote the yield point and the onset of fibrillation, respectively. **c** Cohesive-strength test results. **d–f** SEM images of samples containing bimodal SiO_2 particles with size combinations of (**d**) 10+10 μm, (**e**) 10+ 5 μm, and (**f**) 10+1.5 μm. **g** Mercury intrusion porosimetry results for dry films prepared with bimodal SiO_2 particles of different median sizes. **h–j** Schematic of particle–binder interaction in bimodal systems. **(h)** Unimodal system. **(i)** Enhanced fibrillation (bimodal system with appropriate particle size combination). **(j)** Insufficient fibrillation (bimodal system with inappropriate particle size combination).

Inverse design of PLP and particle size for PTFE fibrillation

Although our particle dynamics analysis revealed the relationship between particle size and PTFE fibrillation, bridging this understanding to practical process conditions required further optimization. To this end, we trained a GPR model using data from a parametric analysis considering the particle size and PLP as inputs. The final P_{lm} and final strain values from each simulation's S-S curve were used as the output variables as these represent the final deformation state of the PTFE. The trained GPR model validated through *k*-fold cross-validation (R^2 values of 0.989 and 0.995 for unimodal and bimodal systems, respectively) was integrated into a Bayesian optimization framework to systematically identify the optimal PLP conditions across particle sizes. The optimization objective was to maximize the final strain, subject to the PTFE material constraints ($P_{\mathrm{lm}} < 45$ MPa, $strain < 4$). The resulting contour maps shown in **Fig. 5** provided optimal PLP–particle size regions. For the unimodal system, particle sizes between 1.5 and 10 μm were explored, with representative Bayesian optimization results shown for a fixed PLP of 13 MPa (**Fig. 5a**) and a fixed particle size of 10 μm (**Fig. 5b**). Similarly, for the bimodal system, combinations of particles in the range from 3 to 10 μm were investigated to identify favorable fibrillation conditions, as exemplified by the results at a fixed PLP of 13 MPa (**Fig. 5d**) and a fixed particle size combination of 10+5 μm (**Fig. 5**). This integrated framework enabled the inverse design of optimal particle size and PLP conditions to enhance PTFE fibrillation efficiency and guide granule formation.

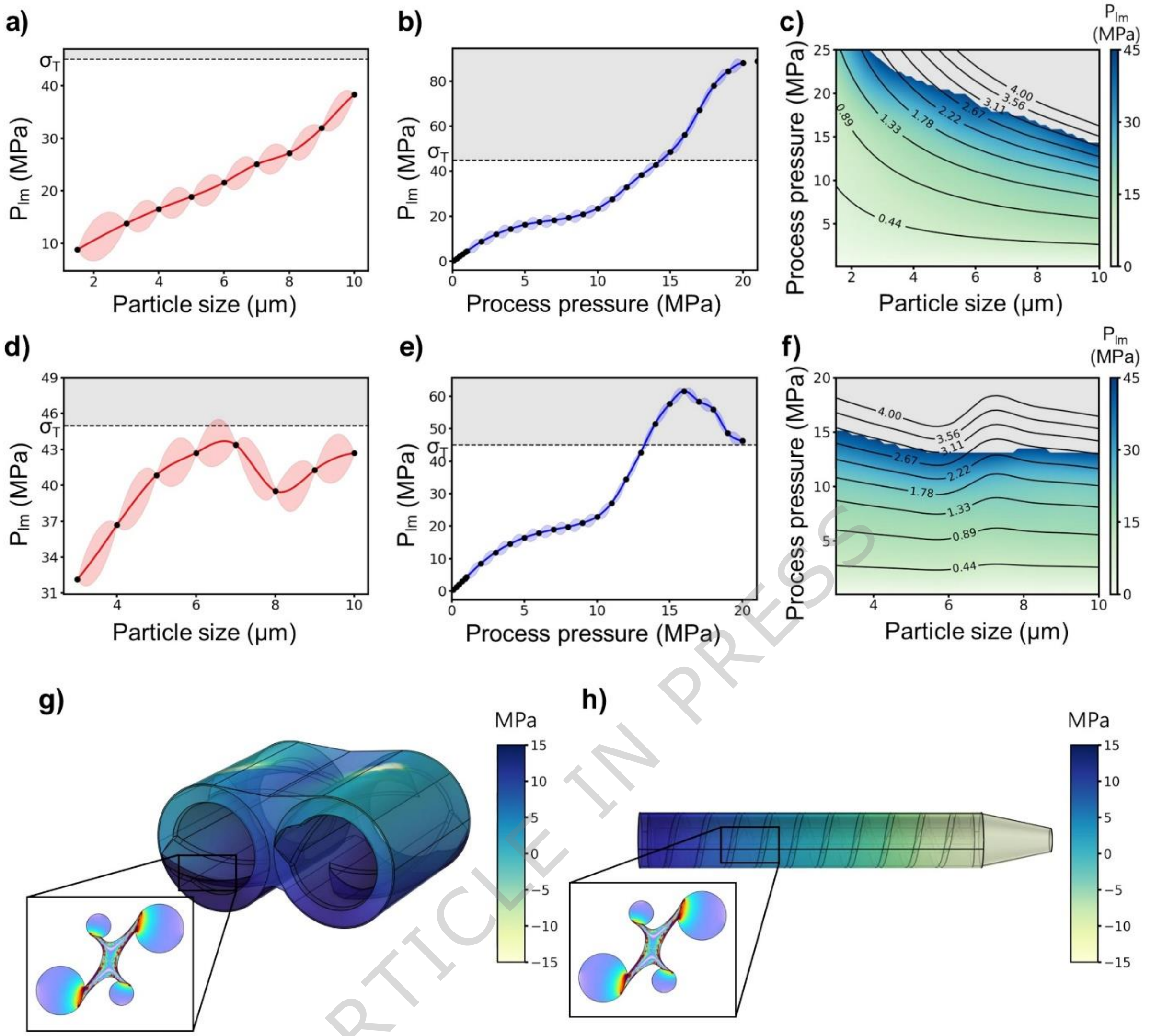

Fig. 5 | Optimization and inverse design of particle size and PLP conditions for efficient PTFE fibrillation.

a Bayesian optimization results for unimodal system at fixed PLP of 13 MPa. **b** Bayesian optimization results for unimodal system at fixed particle size of 10 µm. **c** Contour plot of Bayesian optimization results for unimodal system, showing the relation between PLP and particle size. The black contour lines represent the final strain, while the color map represents the final P_{lm}. **d** Bayesian optimization results for bimodal system at fixed PLP of 13 MPa. **e** Bayesian optimization results for bimodal system at fixed particle size combination of 10+5 µm. **f** Contour plot of Bayesian optimization results for bimodal system, showing the optimal PLP–particle size ranges. The black contour lines represent the final strain, while the color map represents the final P_{lm}. **g** FEM model of kneader, showing shear stress distribution. **h** FEM model of extruder, showing shear stress profile along extrusion pathway.

PLP originates from processing equipment such as a kneader or extruder, which primarily controls macroscale parameters including the rotational speed and equipment geometry. Therefore, inverse design should incorporate macroscale features. Hence, we developed multiscale FEM models as illustrated in **Figs. 5g and h.** The parameters of the kneader model were based on the experimental equipment used in this study, whereas the extruder model adopted was based on the literature.[36] Shear stress was calculated using the power-law model for non-Newtonian fluids[37] given as

$$\tau = K\dot{\gamma}^{n}, \tag{1}$$

where K is the fluid consistency index, n is the flow index, and $\gamma^{\cdot}$ is the shear rate. Shear rates obtained from macroscale simulations were subsequently converted into PLP values, serving as initial conditions for particle dynamics simulations. By combining these simulations with the GPR model developed earlier with multiscale approaches, we systematically optimized macroscale processing parameters.

We accurately predicted the optimal rotational speed conditions per particle size required to induce PTFE fibrillation during the dry process. In the unimodal system (**Fig. 5c**), larger particle sizes require lower shear stress to initiate fibrillation. In particular, the 10 μm particle size, which exhibits the most effective fibrillation behavior, requires approximately 14 MPa of shear stress. For the bimodal system (**Fig. 5f**), the analysis provides a more detailed inference for the optimal particle configuration. The Bayesian optimization, aimed at maximizing induced strain, revealed that the top-three performing secondary particle sizes were 4.5, 5.0, and 6.0 μm. Based on these results, we infer the optimal range for the secondary particle to be between 4.5 and 6.0 μm, which requires a shear stress in the range of 13.5–14.7 MPa for effective fibrillation. Our simulation framework can be used to translate these shear stress requirements into practical process conditions. A kneader speed of 10 rpm (13.49 MPa) and extruder speed of 700 rpm (13.6 MPa) are determined as the optimal parameters for promoting PTFE fibrillation in both the 10 μm unimodal system and 10–5 μm bimodal system. Accordingly, we propose the 10+5 μm bimodal configuration combined with a kneader speed of 10 rpm as the optimal conditions for efficient PTFE fibrillation.

To apply our findings to practical electrode materials, the simulation results using SiO_2 were extended to $LiFePO_4$ (LFP), which shares similar morphological characteristics, particularly the spherical shape and fine particle distribution. As PTFE fibrillation is strongly influenced by the particle morphology, including shape and surface characteristics, as demonstrated in previous studies, the morphological similarity allows to transfer simulation-based insights from the SiO_2 system to the LFP system.[12,38] This transferability can be validated by comparing the SS curves of PTFE in contact with 10 μm SiO_2 and LFP particles, which exhibit comparable fibrillation behavior (**Supplementary Fig. 6**). This analysis indicates that the PTFE fibrillation mechanism observed in the SiO_2 system is also applicable to the LFP system. Accordingly, inverse process design was developed to determine the optimal LFP particle size distribution and kneading conditions, leading to the selection of 5 and 10 μm particles, as shown in **Fig. 6a.**

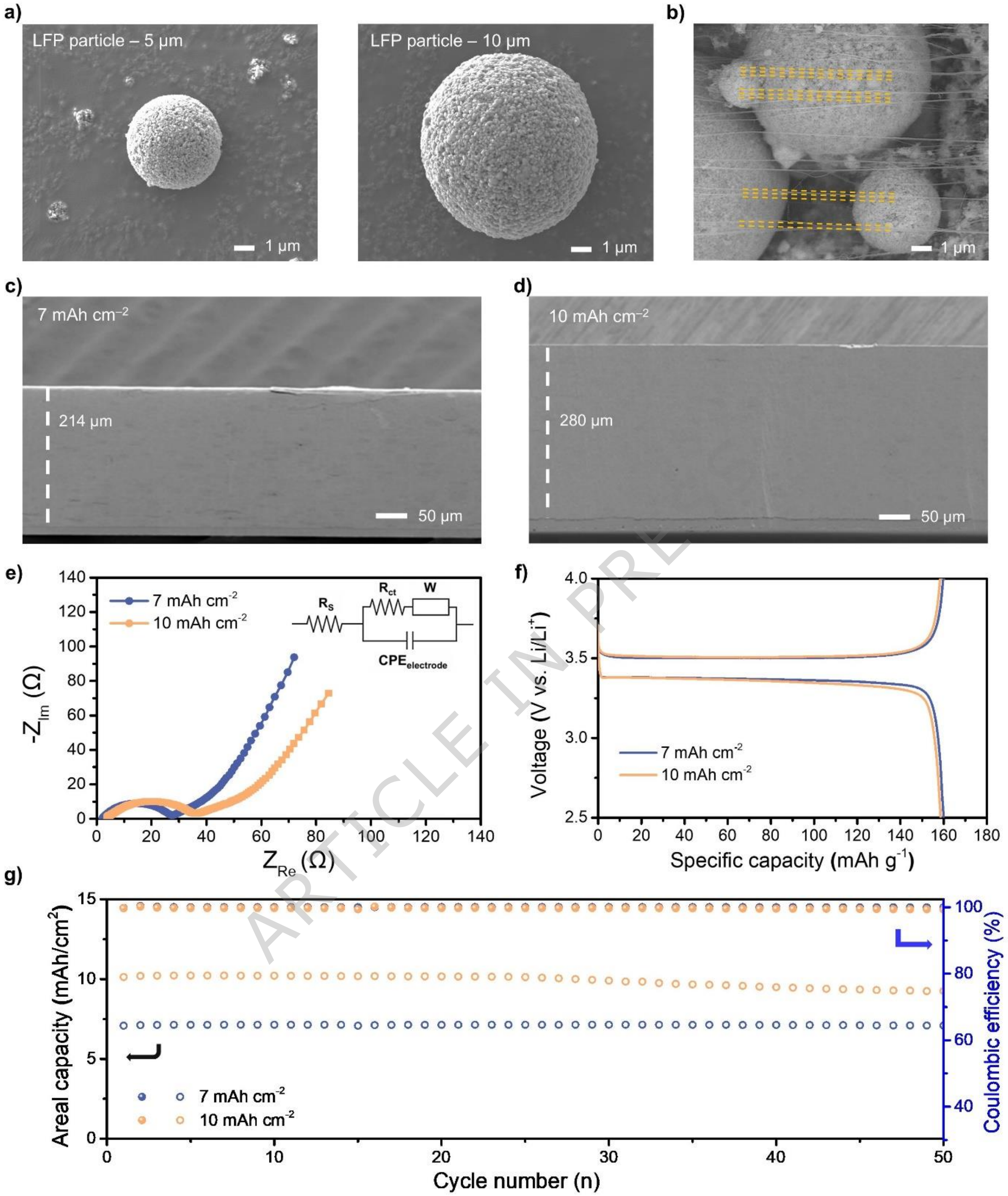

Fig. 6 | Structural and electrochemical characterization of optimized dry-processed bimodal LFP cathodes. **a** SEM images of LFP active material distinct particle size of 5 μm and 10 μm, respectively. **b** PTFE fibrillar network formed under optimized dry-processing conditions. **c** Cross-sectional SEM images of electrodes with area capacities of 7 mAh cm^{-2}. **d** Cross-sectional SEM images of electrodes with area capacities of 10 mAh cm^{-2}. **e** Charge-transfer resistance (R_{ct}) of cathodes with area capacities of 7 and 10 mAh cm^{-2}. **f** first-cycle voltage profiles. **g** Cycling performance over 50 cycles for cathodes with area capacities of 7 and 10 mAh cm^{-2}.

Structural and electrochemical evaluation of optimized dry-processed electrode

To validate the design experimentally, dry-processed LFP electrodes were fabricated using the 10–5 μm bimodal particle combination identified through inverse modeling. Under optimized conditions, PTFE forms a uniform fibrous network that reinforces interparticle binding and mechanical cohesion, as shown in **Fig. 6b**. In cross-sectional SEM images, the cathodes with area capacities of 7 and 10 mAh cm^{-2} exhibited dense and uniform microstructures with thicknesses of 214 and 280 μm, respectively (**Figs. 6c and 6d**). The cathode with an areal capacity of 10 mAh cm^{-2} exceeds the conventional thickness range, highlighting the importance of structural integrity.[39] Under this high-loading condition, the dry-processed cathode maintains uniform lamination without visible cracks, as shown in **Supplementary Figs. 7a** and **b**. In contrast, the wet-processed cathode exhibits severe surface cracking at a mass loading of 48.47 mg cm^{-2} due to binder migration during solvent drying (**Supplementary Fig. 7c**). The electrochemical impedance spectroscopy (EIS) results shown in **Fig. 6e** reveal a slight increase in charge-transfer resistance (R_{ct}) with measurements of 25.84 and 33.42 Ω for the cathodes with areal capacities of 7 and 10 mAh cm^{-2}, respectively. Although thicker electrodes generally exhibit substantially increased R_{ct} owing to extended ion diffusion pathways,[40] the observed increase is small. These results suggest that well-developed PTFE fibrillation enhances the electrode structural stability, increasing the ion-transport efficiency. **Fig. 6f** shows the first-cycle voltage profiles of both cathodes. According to previous studies, increasing the slurry loading of LFP electrodes can lead to a voltage hysteresis (ΔV) up to 0.22 V.[41] In contrast, both cathodes fabricated under optimized dry-processing conditions exhibited consistent voltage profiles, with a nominal capacity plateau near 3.43 V and low hysteresis ΔV. This behavior reflects reduced overpotential during charge–discharge, attributed to the low resistance R_{ct} of the structurally stable bimodal dry-processed electrodes. As shown in **Fig. 6g**, both cathodes maintained over 99% Coulombic efficiency and stable capacity over 50 cycles. The cathode with an areal capacity of 10 mAh cm^{-2} exhibited no degradation under high-loading conditions. Hence, the proposed process enables PTFE fibrillation and stable operation of thick dry-processed electrodes.

Conclusions

This study aimed to bridge the gap between the PTFE fibrillation mechanism, influenced by particle size effects, and practical process optimization by employing a multiphysics FEM model and AI-based optimization. We found that the PTFE fibrillation efficiency in dry electrode processing depends significantly on the particle size distribution. We identified methods to evaluate the optimal particle size in unimodal and bimodal configurations. For a bimodal system, combining large- and intermediate-sized particles substantially enhanced fibrillation. Based on the particle dynamics and macroscale FEM simulation, we developed an optimization method for the equipment and experimentally demonstrated its enhanced fibrillation and electrochemical properties. Our research provides a valuable framework for systematically linking particle dynamics modeling, practical process optimization, and experimental validation, contributing to the advancement of dry-process electrode manufacturing.

Methods

PTFE deformation simulation

FEM simulations were conducted using the *Nonlinear Elastic Material* module in COMSOL Multiphysics to investigate the relationship between particle size and PTFE deformation. Detailed simulation parameters are presented in **Supplementary Table S1**. The material properties for PTFE, F-106, including the tensile strength and elongation, were obtained from the manufacturer's technical datasheet. The fundamental elastic properties, specifically the Young's modulus and Poisson's ratio, were obtained from established experimental data in the paper.[42] To model the nonlinear deformation behavior of PTFE, the Arruda-Boyce model was chosen due to its capability to accurately capture the finite extensibility of polymer chains. This model is based on the eight-chain molecular network theory, where the Helmholtz free energy is derived from the inverse Langevin function. The governing equations are given as follows:

$$\rho \frac{\partial^2 u}{\partial t^2} = \nabla \cdot (FS)^T + Fv \tag{2}$$

$$F = I + \nabla \mu \tag{3}$$

Here ρ is the density, u is the displacement, t is time, F is the strain, S is the stress, v is the volume force. To account for the strain energy density function, the model follows the form:

$$W_s = \mu_0 \sum_{p=1}^{5} \frac{C_p}{N^{p-1}} \left(\lambda_1^p + \lambda_2^p + \lambda_3^p\right) + \frac{1}{4} K(J_{el}^2 - 1 - 2\ln(J_{el})) \tag{4}$$

W_s is deformation energy, C_p is material constant based Langevin function, λ is the effective stretch of polymer chain, K is bulk modulus, is J_{el} Jacobian determinant. The first term (left side of the equation, summation term) corresponds to the plastic deformation region, which accounts for the entropic elasticity of polymer chains. The second term (right side of the equation, volume correction term) represents the elastic deformation region, which governs the bulk modulus and volumetric response of the material. We employed Simo-Taylor, the model efficiently captures large-strain hyperelastic behavior, making it well-suited for simulating polymeric materials and elastomers under finite deformation.

Kneader and Extruder simulation

To investigate the shear stress generated during kneader and extruder processing, we employed the *Fluid Flow Module* and *Heat Transfer in Fluids Module* in COMSOL Multiphysics. To replicate the actual process conditions validated by our in-situ monitoring, the model's thermal boundary conditions were precisely defined: a controlled temperature of 80 ℃ was applied to the chamber walls, while convective heat flux was used to model heat loss from external surfaces to the ambient (25 ℃) environment. The geometry of the kneader was modeled to match the specifications of the experimental equipment (**Supplementary Fig. 2**). The detailed simulation parameters are presented in **Supplementary Table S2**. The governing equations for fluid dynamics are based on the Navier-Stokes equations:

$$0 = \nabla \cdot [-pl + K] + F \tag{5}$$

$$\rho \nabla \cdot \mu = 0 \tag{6}$$

Here p is the pressure, K is the stress tensor includes viscous, F is the external force, ρ is the fluid density, μ is the velocity. The electrode granule was modeled as a non-Newtonian fluid to account for its rheological behavior during processing.

To incorporate the effect of process temperature on electrode granule properties, we applied the heat transport equation:

$$\rho C_p \mu \cdot \nabla T + \nabla \cdot q = Q + Q_p + Q_{vd} \tag{7}$$

C_p is the specific heat capacity, T is the temperature, q is the heat flux, Q is the external heat source. Heat transfer was described using Fourier's law of heat conduction:

$$q = -k\nabla T \tag{8}$$

where k is the thermal conductivity.

GPR model and Bayesian optimization

The dataset for PTFE fibrillation optimization was constructed using simulation data generated from FEM modeling. Particle size and PLP were selected as the primary input parameters, while the corresponding P_{lm} and strain values were used as output variables.

To ensure reliable predictions, we employed GPR to model the relationship between input parameters and fibrillation behavior. The Matérn kernel was used to effectively capture nonlinear relationships in physical systems, and hyperparameters were optimized through maximum likelihood estimation (MLE). The entire dataset was used to train the GPR model without explicit division into training and test sets.

Once the GPR model was trained, Bayesian optimization was applied to systematically determine the optimal PLP conditions for each particle size. The optimization process considered the mechanical limitations of PTFE by setting constraints on stress and strain values. The trained model's accuracy was assessed by comparing its predictions with FEM simulation results, ensuring consistency with previous experimental observations. This approach provided a structured framework for linking microscale particle dynamics with practical process conditions, ultimately guiding the optimization of PTFE fibrillation in the dry process.

Electrode preparations

Dry electrodes were fabricated on a 150 g batch scale. SiO_2 particles with different PSDs were used as the main component, including small particles (0.1, 1.5, and 5 μm), large particles (10 and 20 μm), and bimodal mixtures of small and large particles. LFP was also employed as active material with particle sizes of 5 and 10 μm, including their bimodal combinations. Carbon black (CB, Super P) and PTFE (F-106, Daikin Industries) were used as the conductive additive and binder, respectively. All components were mixed at a weight ratio of 90:5:5 (AM:conductive additive:binder).

The electrode fabrication consisted of three steps. In the first step, the powder components were mixed using a high-shear rotary mixer (PLS-300, KMTECH) under controlled shear stress and time conditions to ensure uniform dispersion. In the second step, fibrillation was induced to transform the PTFE binder into fibrous networks that bridge the active material and conductive additive. This step was conducted using an extruder (NEP-0.5K, KMTECH) and a crusher (PLS-300, KMTECH). In the third step, free-standing dry films were fabricated. The fibrillated powder mixture was passed through a roller press (KRM-100D3, KMTECH), and the resulting sheets were calendered using a roll press to achieve the target thickness. The final electrodes were laminated onto carbon-coated aluminum current collectors to complete electrode fabrication. The mass loading of the electrodes was controlled to 43 and 69 mg cm^{-2}, corresponding to areal capacities of 7 and 10 mAh cm^{-2}, respectively. The target electrode density was maintained at 2.3 g/cc. The wet-processed electrode with an areal capacity of 7 mAh cm^{-2} was fabricated using a conventional slurry-casting method. A total of 20 g of slurry was prepared by dispersing bimodal LFP, CB, and polyvinylidene fluoride binder in N-methyl-2-pyrrolidone at a mass ratio of 90:5:5. The slurry was then cast onto an aluminum foil current collector using a doctor blade and dried in a vacuum oven at 80 °C overnight to ensure complete solvent removal.

Cell assembly

Coin-type cells (CR2032, Wellcos Corporation) were assembled in a dry room with a controlled dew point below −50 °C. A polyethylene separator was used to isolate the electrodes. For half-cell configurations, electrochemical performance was evaluated using Li metal foil as the counter electrode and an electrolyte consisting of 1.15 M $LiPF_6$ dissolved in a solvent mixture of ethylene carbonate, ethyl methyl carbonate, and diethyl carbonate in a 2:4:4 volume ratio. The electrolyte was further modified with 1 wt% vinylene carbonate, 10 wt% fluoroethylene carbonate, and 1 wt% lithium difluorophosphate.

Material and electrochemical characterization.

The cohesive strength of the dry-processed electrode sheets with different PSDs was evaluated using a UTM, (Autograph AGS-X, SHIMADZU). These measurements were performed to assess the mechanical integrity of the electrodes as a function of active material particle size. Galvanostatic charge–discharge tests were conducted using a battery cycler (WBCS3000L32, WonATech, South Korea) to assess the electrochemical performance of the dry-processed electrodes. To confirm the PSD of SiO_2 used as the model active material in FEM simulations, measurements were performed using a laser scattering particle size distribution analyzer (LA-950, HORIBA, Japan), which enables reliable evaluation of various particle size distributions. Prior to measurement, the SiO_2 samples were dispersed in distilled water and treated with ultrasonication to prevent agglomeration. The porosity of the free-standing dry electrodes was measured using mercury intrusion porosimetry (Automatic Porosimeter, AutoPore IV, Micromeritics, USA). For each measurement, approximately 0.4 g of sample was loaded. The analysis was performed over a pressure range of 0.10–60,000 psia, with the following parameters: evacuation pressure of 50 Torr Hg, evacuation time of 10 min, mercury filling pressure of 0.43 psia, and equilibration time of 10 s at both low- and high-pressure stages. This method enabled quantitative determination of the pore size distribution and total porosity of the electrodes. All half-cell measurements were performed under a constant current–constant voltage (CC–CV) protocol at a rate of 0.1C within the voltage range of 2.5–4.0 V versus Li/Li^+. EIS was conducted using a Biologic VSP potentiostat (Seyssinet-Pariset, France) by applying a sinusoidal voltage of 5 mV over the frequency range of 250 kHz to 10 mHz.

Data availability

The data that support the findings of this study are available from the corresponding authors upon reasonable request.

Email: Junghyun Choi (junghchoi@gachon.ac.kr), Sung Beom Cho (csb@ajou.ac.kr)

Code availability

Codes used to generate the simulation result in this study are available in the Supplementary Code file.

References

1. Chen, X., Shen, W., Vo, T. T., Cao, Z. & Kapoor, A. An overview of lithium-ion batteries for electric vehicles. *2012 10th Int. Power Energy Conf. (IPEC)* 230–235 (2012) doi:10.1109/asscc.2012.6523269.

2. Li, J. *et al.* Toward low-cost, high-energy density, and high-power density lithium-ion batteries. *JOM* **69**, 1484–1496 (2017).

3. Chouchane, M., Yao, W., Cronk, A., Zhang, M. & Meng, Y. S. Improved rate capability for dry thick electrodes through finite elements method and machine learning coupling. *ACS Energy Lett.* **9**, 1480–1486 (2024).

4. Jeon, D. H. Wettability in electrodes and its impact on the performance of lithium-ion batteries. *Energy Storage Mater.* **18**, 139–147 (2019).

5. Kim, S. *et al.* Scalable dry process for fabricating a Na superionic conductor-type solid electrolyte sheet. *ACS Appl. Mater. Interfaces* **16**, 10307–10315 (2024).

6. Wang, J. *et al.* High-area-capacity cathode by ultralong carbon nanotubes for secondary binder-assisted dry coating technology. *ACS Appl. Mater. Interfaces* **16**, 26209–26216 (2024).

7. Lee, J. *et al.* Anode interface-stabilizing dry process employing a binary binder system for ultra-thick and durable battery electrode fabrication. *Chem. Eng. J.* **503**, 158271 (2025).

8. Kim, J. *et al.* 10 mAh cm^{-2} cathode by roll-to-roll process for low cost and high energy density Li-ion batteries. *Adv. Energy Mater.* **14**, (2024).

9. Han, S. *et al.* Mitigating PTFE decomposition in ultra thick dry-processed anodes for high energy density lithium-ion batteries. *J. Energy Storage* **96**, 112693 (2024).

10. Kim, N.-Y. *et al.* Material challenges facing scalable dry-processable battery electrodes. *ACS Energy Lett.* **9**, 5688–5703 (2024).

11. Kim, H. *et al.* Ozone-treated carbon nanotube as a conductive agent for dry-processed lithium-ion battery cathode. *ACS Energy Lett.* **8**, 3460–3466 (2023).

12. Horst, M. *et al.* Effect of active material morphology on PTFE-fibrillation, powder characteristics and electrode properties in dry electrode coating processes. *Powder Technol.* **451**, 120451 (2025).

13. Zhang, A. *et al.* Fibrosis mechanism, crystallization behavior and mechanical properties of in-situ fibrillary PTFE reinforced PP composites. *Mater. Des.* **211**, 110157 (2021).

14. Li, Y. *et al.* Progress in solvent-free dry-film technology for batteries and supercapacitors. *Mater. Today* **55**, 92–109 (2022).

15. Lee, D. *et al.* Shear force effect of the dry process on cathode contact coverage in all-solid-state batteries. *Nat. Commun.* **15**, 4763 (2024).

16. Oh, H. *et al.* Development of a feasible and scalable manufacturing method for PTFE-based solvent-free lithium-ion battery electrodes. *Chem. Eng. J.* **491**, 151957 (2024).

17. Matthews, G. A. B., Wheeler, S., Ramírez-González, J. & Grant, P. S. Solvent-free NMC electrodes for Li-ion batteries: unravelling the microstructure and formation of the PTFE nano-fibril network. *Front. Energy Res.* **11**, 1336344 (2024).

18. Yonaga, A. *et al.* Effects of dry powder mixing on electrochemical performance of lithium-ion battery electrode using solvent-free dry forming process. *J. Power Sources* **581**, 233466 (2023).

19. Tao, R. *et al.* Unraveling the impact of the degree of dry mixing on dry-processed lithium-ion battery electrodes. *J. Power Sources* **580**, 233379 (2023).

20. Patil, P. D., Feng, J. J. & Hatzikiriakos, S. G. Constitutive modeling and flow simulation of polytetrafluoroethylene (PTFE) paste extrusion. *J. Non-Newton. Fluid Mech.* **139**, 44–53 (2006).

21. Li, Y. *et al.* Progress in solvent-free dry-film technology for batteries and supercapacitors. *Mater. Today* **55**, 92–109 (2022).

22. Kang, J. *et al.* Tough-interface-enabled stretchable electronics using non-stretchable polymer semiconductors and conductors. *Nat. Nanotechnol.* **17**, 1265–1271 (2022).

23. Khan, A. & Zhang, H. Finite deformation of a polymer: experiments and modeling. *Int. J. Plast.* **17**, 1167–1188 (2001).

24. Bergström, J. S. & Hilbert, L. B. A constitutive model for predicting the large deformation thermomechanical behavior of fluoropolymers. *Mech. Mater.* **37**, 899–913 (2005).

25. Schulz, E., Speekenbrink, M. & Krause, A. A tutorial on Gaussian process regression: Modelling, exploring, and exploiting functions. *J. Math. Psychol.* **85**, 1–16 (2018).

26. Zhang, J. *et al.* Dual-objectives optimization of lithium metal battery electrolytes via machine learning. *Mater. Today Energy* 101909 (2025) doi:10.1016/j.mtener.2025.101909.

27. Frazier, P. I. A Tutorial on Bayesian Optimization. *arXiv* (2018) doi:10.48550/arxiv.1807.02811.

28. Arruda, E. M. & Boyce, M. C. A three-dimensional constitutive model for the large stretch behavior of rubber elastic materials. *J. Mech. Phys. Solids* **41**, 389–412 (1993).

29. Lan, T. *et al.* A physically-based constitutive model for amorphous glassy polymers in large deformations. *Eur. J. Mech. - ASolids* **104**, 105015 (2024).

30. Hong, S. B., Kim, J., Gu, N. S. & Yu, W.-R. Constitutive modelling of carbon fiber-reinforced shape memory polymer composites. *J. Phys.: Conf. Ser.* **1063**, 012028 (2018).

31. Kanarik, K. J. *et al.* Human–machine collaboration for improving semiconductor process development. *Nature* **616**, 707–711 (2023).

32. Luo, C., Pei, J., Zhuo, W., Niu, Y. & Li, G. Phase transition behavior and deformation mechanism of polytetrafluoroethylene under stretching. *RSC Adv.* **11**, 39813–39820 (2021).

33. Zhang, Y., Jar, P.-Y. B., Xue, S. & Li, L. Quantification of strain-induced damage in semi-crystalline polymers: a review. *J. Mater. Sci.* **54**, 62–82 (2019).

34. Fujitani, K., Utsumi, Y., Yamaguchi, A., Sumida, H. & Suzuki, S. Preferential side chain scission of polytetrafluoroethylene by bending stress. *Appl. Surf. Sci*. **637**, 157891 (2023).

35. Park, S. K., Kim, K. D. & Kim, H. T. Preparation of silica nanoparticles: determination of the optimal synthesis conditions for small and uniform particles. *Colloids Surf. A: Physicochem. Eng. Asp*. **197**, 7–17 (2002).

36. Haarmann, M., Grießl, D. & Kwade, A. Continuous Processing of Cathode Slurry by Extrusion for Lithium-Ion Batteries. *Energy Technol.* **9**, (2021).

37. Lavrov, A. Numerical modeling of steady-state flow of a non-Newtonian power-law fluid in a rough-walled fracture. *Comput. Geotech.* **50**, 101–109 (2013).

38. Hwang, J. H., Yoo, H., Oh, S. & Kim, H. Relationship between particle shape and fast-charging capability of a dry-processed graphite electrode in lithium-ion batteries. *Electrochem. Commun.* **165**, 107761 (2024).

39. Kim, Y. *et al.* Investigation of mass loading of cathode materials for high energy lithium-ion batteries. *Electrochem. Commun.* **147**, 107437 (2023).

40. Shi, Y. *et al.* Tortuosity modulation toward high-energy and high-power lithium metal batteries. *Adv. Energy Mater.* **11**, (2021).

41. Kwon, K. *et al.* Low-resistance $LiFePO_4$ thick film electrode processed with dry electrode technology for high-energy-density lithium-ion batteries. *Small Sci.* **4**, (2024).

42. Bi, Z. & Mueller, D. W. Friction predication on pin-to-plate interface of PTFE material and steel. *Friction* **7**, 268–281 (2019).

Acknowledgements

This research was supported by the National R&D Program through the National Research Foundation of Korea (NRF) funded by the Ministry of Science and ICT (No. RS-2024-00408156). This research was also supported by the National R&D Program through the NRF funded by the Ministry of Science and ICT (RS-2024-00407282).

Author contributions

J.H.K. and W.J. contributed equally to this work. J.H.K.: Writing – original draft, Conceptualization, Methodology, Software, Investigation, Formal analysis, Visualization. W.J.: Writing – original draft, Methodology, Investigation, Validation, Formal analysis. M.S.K.: Software, Formal analysis. H.W.K.: Visualization. D.W.J.: Formal analysis, Visualization. H.U.L.: Visualization. J.H.H.: Visualization. S.H.: Investigation, Validation. M.K.: Investigation, Validation. S.Y.: Investigation, Validation. D.L.: Supervision. P.J.K.: Supervision. T.S.: Supervision. M.Y.: Supervision. L.S.: Supervision. J.C.: Writing – review & editing, Supervision, Funding acquisition, Project administration. S.B.C.: Writing – review & editing, Supervision, Funding acquisition, Project administration.

Competing interests

The authors declare no conflict of interest.

Figure Captions

Fig. 1 | Multiscale inverse design framework for optimizing PTFE fibrillation in dry electrode processing.
a Schematic illustration of the dry electrode manufacturing process and the effect of PTFE fibrillation on electrode. **b** Workflow of computational process for efficient PTFE fibrillation.

Fig. 2 | Simulation for PTFE deformation. a Schematic of the boundary conditions and initial state in the simulation. **b** SS curve of PTFE illustrating fibrillation evolution and transition to film-like deformation.

Fig. 3 | Correlating FEM-based stress response with experimental validation of unimodal particle size effects. a Frequency distribution of unimodal SiO_2 particles with nominal diameters of 0., 1.5, 10, and 20 μm, measured using a laser-scattering PSD analyzer. **b** SS curves for different SiO_2 particle sizes. The blue area indicates the target fibrillation region, and the gray area represents the failure region leading to film-like deformation. The circle and square symbols on the SS curve denote the yield point and the onset of fibrillation, respectively. **c** Cohesive-strength test results. **d–g** SEM images of samples containing SiO_2 particles with sizes of (**d**) 20, (**e**) 10, (**f**) 1.5, and (**g**) 0.1 µm. **h** Mercury intrusion porosimetry results for dry electrodes prepared with unimodal SiO_2 particles of different median sizes. Reliable porosity measurement for the dry electrode fabricated with 0.1-µm SiO_2 particles was impossible owing to its brittle nature. **i–k** Schematic of the effect of the particle size on the PTFE deformation behavior. **(i)** Film-like deformation. **(j)** Fibrillation. **(k)** Insufficient fibrillation.

Fig. 4 | Correlating FEM-based stress response with experimental validation of bimodal particle size effects. a Frequency distribution of bimodal SiO_2 systems with particle size combinations of 10+1.5 µm and 10+5 µm, measured using a laser-scattering PSD analyzer. **b** SS curves for different SiO_2 particle size combinations. The blue area indicates the target fibrillation region, while the gray area represents the failure region leading to film-like deformation. The circle and square symbols on the SS curve denote the yield point and the onset of fibrillation, respectively. **c** Cohesive-strength test results. **d–f** SEM images of samples containing bimodal SiO_2 particles with size combinations of (**d**) 10+10 µm, (**e**) 10+ 5 µm, and (**f**) 10+1.5 µm. **g** Mercury intrusion porosimetry results for dry films prepared with bimodal SiO_2 particles of different median sizes. **h–j** Schematic of particle–binder interaction in bimodal systems. **(h)** Unimodal system. **(i)** Enhanced fibrillation (bimodal system with appropriate particle size combination). **(j)** Insufficient fibrillation (bimodal system with inappropriate particle size combination).

Fig. 5 | Optimization and inverse design of particle size and PLP conditions for efficient PTFE fibrillation.

a Bayesian optimization results for unimodal system at fixed PLP of 13 MPa. **b** Bayesian optimization results for unimodal system at fixed particle size of 10 µm. **c** Contour plot of Bayesian optimization results for unimodal system, showing the relation between PLP and particle size. The black contour lines represent the final strain, while the color map represents the final $P_{lm.}$ **d** Bayesian optimization results for bimodal system at fixed PLP of 13 MPa. **e** Bayesian optimization results for bimodal system at fixed particle size combination of 10+5 µm. **f** Contour plot of Bayesian optimization results for bimodal system, showing the optimal PLP–particle size ranges. The black contour lines represent the final strain, while the color map represents the final $P_{lm.}$ **g** FEM model of kneader, showing shear stress distribution. **h** FEM model of extruder, showing shear stress profile along extrusion pathway.

Fig. 6 | Structural and electrochemical characterization of optimized dry-processed bimodal LFP cathodes. **a** SEM images of LFP active material distinct particle size of 5 µm and 10 µm, respectively. **b** PTFE fibrillar network formed under optimized dry-processing conditions. **c** Cross-sectional SEM images of electrodes with area capacities of 7 mAh cm^{-2}. **d** Cross-sectional SEM images of electrodes with area capacities of 10 mAh cm^{-2}. **e** Charge-transfer resistance (R_{ct}) of cathodes with area capacities of 7 and 10 mAh cm^{-2}. **f** first-cycle voltage profiles. **g** Cycling performance over 50 cycles for cathodes with area capacities of 7 and 10 mAh cm^{-2}.

ED summary:

PTFE is a key material for the dry fabrication of battery electrodes, and controlling its fibrillation is key. Here, a computational framework for PTFE fibrillation identifies optimal particle size and particle-loaded pressure, validated by electrode fabrication.

Peer review information:

Communications Materials thanks Qiang Zhang, Victor A. Beck and the other, anonymous, reviewer(s) for their contribution to the peer review of this work. A peer review file is available.